AGU PUBLICATIONS

JGR

Journal of Geophysical Research: Earth Surface

RESEARCH ARTICLE

10.1002/2014JF003293

Key Points:

- Pore pressure grows with wind speed squared and ripple aspect ratio
- Pressure on a porous surface is different than on impermeable solids
- Porosity affects the turbulent boundary layer through slip and surface pressure

Supporting Information:

- Readme
- Text S1
- Text S2

Correspondence to:
M. Y. Louge,
MYL3@cornell.edu

Citation:
Musa, R. A., S. Takarrouht, M. Y. Louge, J. Xu, and M. E. Berberich (2014), Pore pressure in a wind-swept rippled bed below the suspension threshold, *J. Geophys. Res. Earth Surf.*, *119*, doi:10.1002/2014JF003293.

Received 24 JUL 2014
Accepted 23 OCT 2014
Accepted article online 27 OCT 2014

Pore pressure in a wind-swept rippled bed below the suspension threshold

R. A. Musa[1], S. Takarrouht[2], M. Y. Louge[1], J. Xu[1], and M. E. Berberich[1]

[1]Sibley School of Mechanical and Aerospace Engineering, Cornell University, Ithaca, New York, USA, [2]Ecole Polytechnique de l'Université de Nantes, Nantes, France

Abstract Toward elucidating how a wavy porous sand bed perturbs a turbulent flow above its surface, we record pressure within a permeable material resembling the region just below desert ripples, contrasting these delicate measurements with earlier studies on similar impermeable surfaces. We run separate tests in a wind tunnel on two sinusoidal porous ripples with aspect ratio of half crest-to-trough amplitude to wavelength of 3% and 6%. For the smaller ratio, pore pressure is a function of streamwise distance with a single delayed harmonic decaying exponentially with depth and proportional to wind speed squared. The resulting pressure on the porous surface is nearly identical to that on a similar impermeable wave. Pore pressure variations at the larger aspect ratio are greater and more complicated. Consistent with the regime map of Kuzan et al. (1989), the flow separates, creating a depression at crests. Unlike flows on impermeable waves, the porous rippled bed diffuses the depression upstream, reduces surface pressure gradients, and gives rise to a slip velocity, thus affecting the turbulent boundary layer. Pressure gradients within the porous material also generate body forces rising with wind speed squared and ripple aspect ratio, partially counteracting gravity around crests, thereby facilitating the onset of erosion, particularly on ripples of high aspect ratio armored with large surface grains. By establishing how pore pressure gradients scale with ripple aspect ratio and wind speed, our measurements quantify the internal seepage flow that draws dust and humidity beneath the porous surface.

1. Introduction

Winds blowing over desert sand seas create rippled surfaces on porous sand beds [*Bagnold*, 1935, 1942; *Csahók et al.*, 2000; *Andreotti et al.*, 2006; *Creyssels et al.*, 2009; *Charru et al.*, 2013]. As *Kuzan et al.* [1989], *Buckles et al.* [1984], and *Gong et al.* [1996] found in water and air, turbulent flows on wavy surfaces produce pressure variations due to streamline expansion and contraction [*Günther and von Rohr*, 2003]. In permeable sands below the surface, *Louge et al.* [2010b] showed that these variations induce a kind of aeolian-driven "seepage," whereby air penetrates ripple troughs where surface pressure is highest and reemerges at crests, where it is lowest. Although porous media are known to present an unusual boundary condition to external flows [*Beavers and Joseph*, 1967; *Jones*, 1973; *Nield*, 2009], it is unclear how seepage affects a turbulent boundary layer modulated by permeable ripples.

A related question is whether seepage causes porous ripples to act as a significant sink of aeolian dust below the sand suspension threshold. As long as wind speed is not fast enough to mobilize the more compact base on which ripples travel, *Louge et al.* [2010a] predicted that despite its small velocity, seepage entrains dust below ripple troughs by a peculiar capture mechanism that is *enhanced* by wind, whereas conventional dust deposition processes arise with *weakening* wind and reduced turbulence [*Pye and Tsoar*, 1987; *Goossens*, 1988]. A similar process brings benthic nutrients through underwater ripples [*Meysman et al.*, 2007; *Huettel et al.*, 2007; *Fries and Taghon*, 2010]. It may also contribute to hyporheic flow in river beds [*Boulton et al.*, 1998; *Sophocleous*, 2002] and seepage in lake sediments [*Olsthoorn et al.*, 2012]. Although predicted by theory, this dust sequestration mechanism has yet to be fully quantified, since it is unknown how the underlying porous medium affects the turbulent flow responsible for the surface pressure variations that drive seepage.

Louge et al. [2010a] also suggested that the threshold for the onset of aeolian transport, which had hitherto been exclusively associated with the shearing of surface grains [*Bagnold*, 1935; *Shields*, 1936], could be lowered by seepage-induced body forces, as pore pressure gradients within specific regions of the wavy permeable bed help relieve part of its weight. To establish whether these forces affect the transport threshold, it is necessary to quantify the pressure field that the turbulent flow induces within the permeable bed.

Because numerical simulations rely on turbulence closures in the free stream [*Zedler and Street*, 2001; *Chan et al.*, 2007b; *Prinos et al.*, 2003] and on semiempirical boundary conditions at the porous surface [*Beavers and Joseph*, 1967; *Chan et al.*, 2007a], they are no substitute for experiments to evaluate the pore pressure field within a permeable wavy bed. For example, while *Cardenas and Wilson* [2007] simulated the one-way coupling from main flow to seepage, they did not consider conversely how the porous substrate affects the main flow. On the dune scale, such omission is legitimate. However, as the simulations of *Chan et al.* [2007a, 2007b] and the experiments of *Manes et al.* [2009, 2011] showed for flat surfaces, substrate porosity can modify the turbulent boundary layer. Recently, [*Blois et al.*, 2014] used particle-imaging-velocimetry to demonstrate that flows over porous triangular bed forms of coarse gravel differ significantly from those over impermeable surfaces of similar geometry. For these highly separated flows, they noted that the permeable bed thwarts reattachment of the boundary layer by letting fluid pass through its interior. Therefore, it is likely that a porous surface affects turbulence on the ripple scale. Yet it remains unclear whether such effect is limited to coarse beds.

Meanwhile, there exists a mature literature on turbulent flows over impermeable sinusoidal surfaces that includes experiments [*Kendall*, 1970; *Gong et al.*, 1996; *Buckles et al.*, 1984], theory [*Kroy et al.*, 2002; *Fourrière*, 2009; *Fourrière et al.*, 2010], numerical simulations [*Henn and Sykes*, 1999], and stability analyses [*Richards*, 1980; *Engelund and Fredsøe*, 1982; *Mutlu Sumert and Bakioglu*, 1984; *Charru et al.*, 2013]. Most of these studies focused upon variations of the surface shear stress. Although there are limited measurements of mean surface pressure [*Kendall*, 1970; *Buckles et al.*, 1984; *Henn and Sykes*, 1999], no experiment or simulation has yet involved a porous sinusoidal substrate. Intriguingly, *Gong et al.* [1996] observed that surface pressure on an impermeable sinusoidal surface with aerodynamic roughness $\xi_0 \simeq 400$ μm is significantly smaller than on a smoother one with $\xi_0 \simeq 30$ μm, thus bringing to light the role played by microscopic surface features.

In short, it is unclear how porosity affects the turbulent boundary layer above a rippled surface. This raises the following questions: (1) Does porosity modify the surface pressure gradient that drives the flow and, if so, for what size of bed particles? (2) In light of differences between the rough and smooth data of *Gong et al.* [1996], what is the magnitude of pressure variations on a porous substrate? (3) Are internal pore pressure gradients sufficient to produce seepage-induced dust sequestration beneath ripple troughs? (4) By relieving gravity, could these gradients affect the threshold for aeolian transport, traditionally attributed to surface shear stress alone? (5) What is the role of ripple aspect ratio?

To address these questions, we used a wind tunnel to record the pore pressure field within two artificial porous media with sinusoidal surface of wavelength $\lambda = 100$ mm and half vertical trough-to-crest distance $h_0 = 3$ mm and 6 mm. We discerned the role of permeability by comparing our records of pressure on a porous surface to similar measurements on impermeable sinusoidal walls, the only shape for which such data have been published. As we discuss in this article, variations of surface pressure and shear stress scale with the aspect ratios h_0/λ, which is half the inverse of the "ripple index" RI $\equiv \lambda/(2h_0)$.

Ripples feature a wide variety of shapes that are normally asymmetric [*Tanner*, 1967]. However, when h_0/λ is small, their cross section can be sinusoidal [*Baas*, 1994; *Louge et al.*, 2010a], likely for the absence of major flow recirculation behind crests. Although aeolian ripples are often triangular with a steeper leeward face, our experiments staged ripples of sinusoidal cross section for three reasons. First, we endeavored to compare them with the mature literature on impermeable waves, which exclusively reported surface pressure on sinusoidal shapes. Second, adopting an asymmetric cross section would have introduced an additional geometrical aspect ratio beside the single parameter h_0/λ, thus multiplying experimental rigs and complicating interpretation. Third, by comparing two sinusoidal ripples straddling a wide range of ripple index, we could gauge how this single parameter affects pressure within the ripple and on its surface, thus informing future modeling of the turbulent boundary layer and its suspension threshold.

2. Experiments

Measurements of pore pressure present exceptional challenges in shifting sands, even below the saltation threshold. First, wind-driven porous media produce tiny signals of only a few pascals amid turbulent

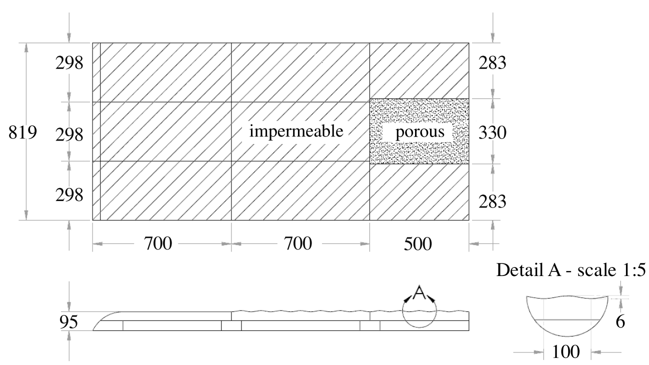

Figure 1. Drawing of the artificial rippled bed with $h_0/\lambda = 3\%$. Dimensions are in millimeters. Flow is from left to right. The rig with $h_0/\lambda = 6\%$ has similar design.

fluctuations. Second, at wind speeds that make pore pressures detectable, erodible sand does not remain in place long enough to fix measurement locations precisely within ripples of millimetric amplitude. In underwater experiments, *Elliott and Brooks* [1997] and *Packman et al.* [2004] observed the flow of tracers through moving bed forms, but they did not measure pressure directly. Therefore, to expose how ripple porosity affects the turbulent boundary layer, our experiments employed a porous plastic with a permeability value that is similar to aeolian sands.

We conducted experiments in the wind tunnel described by *Ribando* [1974] with cross section $\simeq$ 1.2 m wide $\times$ 1 m high, fetch $\simeq$ 12 m, featuring six variable-inlet-guide-vane tube axial exhaust fans of 11 kW, each contributing $\simeq$ 5.5 m/s to the average wind speed U. Thus, to test how robustly pore pressure scales with the kinetic energy density $(\rho/2)U^2$ of air, we explored a wider range of speeds than typically observed in aeolian processes.

The rippled bed sketched in Figure 1 was manufactured on a computer numerical control milling machine. It consisted of three parts: (1) along the flow direction, a developing impermeable RENSHAPE™ plastic section with bluff nose and flat range; (2) transitioning smoothly to the first trough of a similar plastic surface with seven sinusoidal ripples of crestlines perpendicular to the flow, long enough to establish a periodic flow [*Gong et al.*, 1996]; and (3) ending with a porous plastic test section of five full wavelengths with similar cross section around the assembly centerline and flanked on both sides with similar RENSHAPE™ ripples. Although its solid volume fraction $\nu_G \simeq 0.4$ was smaller than a packed granular solid, the porous GENPORE™ plastic had a permeability $K = 3.4 \pm 0.9\ 10^{-11}$ m^2, corresponding to a mean pore diameter $\simeq$ 50 μm, typical of desert sands [*Louge et al.*, 2010b].

To study the role of h_0/λ, we manufactured two similar test beds featuring ripples of $h_0 = 3$ mm and 6 mm, carved in porous plastic with respective thickness $H = 32.5$ mm and 42 mm (Table 1). The aspect ratio $h_0/\lambda = 3\%$ represented the smallest value that would produce detectable pressure signals. (However, as our measurements will indicate, any ripple of smaller aspect ratio should exhibit predictable pore pressure variations scaling with $\rho U^2 h_0/\lambda$.)

We define a 2-D cartesian coordinate system with unit vectors $(\hat{\mathbf{x}}, \hat{\mathbf{y}})$ along the flow and along the *downward* vertical, respectively, with origin in air above the leading trough at an elevation midway between trough and crest, such that the free surface satisfies

$$y = h_0 \cos(2\pi x/\lambda). \tag{1}$$

The third complete trough-crest-trough wavelength downstream of the leading edge of the porous section featured stainless steel tubes of 1.75 mm inside a diameter inserted from below and snugly press fit to the proper depth. The facility with $h_0/\lambda = 3\%$ possessed 36 such tubes and the one with $h_0/\lambda = 6\%$ had 30. The x and y positions of their tips are listed in the supporting information. Each porous test section was bounded underneath by a box enforcing a calm, uniform ambient pressure p_0 on its ceiling located at $y = H$ (Figure 1).

To minimize cross-calibration errors among all pore pressure measurements, the steel tubes were connected to a SCANIVALVE™ (no longer available commercially but equivalent to equipment made by VALCO™ Instruments Co.) that multiplexed them to a single MKS 120-A BARATRON™ differential pressure transducer with $\simeq$1.33 kPa full scale, 10^{-3} Pa resolution and 0.05% reading accuracy. Measurements of pore pressure $(p - p_0)$ relative to the ambient (often called “gauge pressure”) and averaged over 10 s are provided in the supporting information.

To verify that the turbulent boundary layer was fully developed before reaching the rippled section, we recorded vertical profiles of mean air speed above the free surface using a DWYER™ 471-3 hot-wire

Table 1. Experimental Conditions and Harmonic Fits to the Data Using Equation (14)

h_0 (mm)	3	6
λ (mm)	100	100
H (mm)	32.5	42
$A_t \equiv u_*/U$	0.0368 ± 0.0034	0.0383 ± 0.0058
$\bar{p}_1^*$	2.186 ± 0.139	1.057 ± 0.107
$\bar{p}_2^*$		0.371 ± 0.170
$\bar{p}_3^*$		-0.140 ± 0.099
$\bar{p}_a^* - p_0^*$	0.203 ± 0.087	0.085 ± 0.063
$\bar{\phi}_1$ (rad)	-0.186 ± 0.072	-0.499 ± 0.115
$\bar{\phi}_2$ (rad)		-2.28 ± 0.43
$\bar{\phi}_3$ (rad)		-0.02 ± 1.55
$\bar{p}_d^*$	2.2 ± 1.8	3.38 ± 0.38
n	80	90
ϕ_d (rad)	1.57	1.7
$p_{\max}^* - p_0^*$	1.98 ± 0.14	0.71 ± 0.15
$p_{\min}^* - p_0^*$	-2.52 ± 0.20	-2.06 ± 0.31
$F_{\max}$	16.7 ± 1.1	15.1 ± 5.7
$F_{\min}$	-12.5 ± 0.8	-8.7 ± 2.1
P_x^*	0.043 ± 0.016	0.085 ± 0.025
P_y^*	-0.09 ± 0.11	-0.64 ± 0.08
v^*	0.37 ± 0.32	-1.11 ± 0.20

[a]The ratio $A_t \equiv u_*/U$ was recorded just ahead of the rippled section. Pressures marked with an asterisk are made dimensionless using equation (11) assuming $\rho = 1.2$ kg/m^3. $p_{\min}^*$ and $p_{\max}^*$ are their extrema on the surface. Overbars indicate that coefficients were fitted from the average $(p/\rho U^2)(\lambda/h_0)$ among six experiments, each adding one more fan to the previous one. $F_{\min}$ and $F_{\max}$ are minimum and maximum values of F in equation (30) with $\tan\alpha = 0$. P_x^* and P_y^* are dimensionless forces on a unit ripple width in the x and y directions from equations (25) and (26), respectively. v^* is the dimensionless overall seepage into the porous bed through the ceiling of the box at $y = H$ calculated using equation (27). $v^* > 0$ means that the ripple inhales (for $h_0/\lambda = 3\%$) and $v^* < 0$ that it exhales (for $h_0/\lambda = 6\%$). Errors are 95% confidence intervals. In the supporting information, we provide the data used to fit these constants from all pressure taps across six separate wind speeds.

anemometer with vertical resolution $\simeq \pm 1.5$ mm and, wherever the profile conformed to Prandtl's law-of-the-wall, we extracted the shear velocity u_* by fitting data to

$$u = (u_*/\kappa)\ln(z/\xi_0), \tag{2}$$

where z is vertical upward elevation above the mean porous surface, ξ_0 is the "aerodynamic roughness," and $\kappa \simeq 0.41$ is von Kàrmàn's constant. Measurements of time-averaged velocity profiles are provided in the supporting information.

From these profiles, *Buckles et al.* [1984] and *Henn and Sykes* [1999] defined the bulk wind speed U as the mean speed integrated across the channel. Because the turbulent boundary layer is characterized by the shear velocity u_*, one may be tempted to scale pressures with u_* rather than U. However, because shear stress evolves along a slanted surface [*Jackson and Hunt*, 1975; *Kroy et al.*, 2002; *Hersen*, 2004], the bulk speed U, which is invariant along the ripple, is a more robust characteristic of the locally undulating flow.

As Figure 2 illustrates, a turbulent boundary layer with nearly uniform thickness and stable shear velocity was well established before the end of the flat section. Following *Zilker and Hanratty* [1979], we then defined the reference u_* "in terms of the wall shear stress that would exist if the wave section were replaced by a flat section," and we recorded it just ahead of the rippled surface. The right inset in Figure 2 shows that the ratio $A_t \equiv u_*/U$ is a constant, which we list in Table 1. As the same inset shows, the aerodynamic roughness ξ_0 conformed to $\ln(\rho u_* \xi_0/\mu) = -2.45 \pm 0.61$, where $\rho \simeq 1.2$ kg/m^3 and $\mu \simeq 1.8\ 10^{-5}$ kg/m s are, respectively, the density and dynamic viscosity of air. The corresponding values ($0.4 < \xi_0 < 11$ μm) are similar to a typical sand surface. We conducted experiments at conditions summarized in Table 1.

3. Data Reduction

In turbulent boundary layers, pressure fluctuates as bursts with a spectrum of frequencies f [*Willmarth*, 1975]. Bursts of typical size $\ell_b \sim 100\,\mu/(\rho\, u_*)$ [*Kim et al.*, 1971] produce fluctuations at $f \sim u_*/\ell_b = \rho\, U^2 A_t^2/(100\,\mu)$. For our experiments with $3 < U < 36$ m/s, we estimate 10 Hz $\lesssim f \lesssim$ 1.5 kHz. At these relatively low frequencies, it is not necessary to add the inertial terms $[\rho/(1-\nu_G)]\partial v/\partial t$ or $[\rho/(1-\nu_G)]v\partial v/\partial x$ to Darcy's law

$$\nabla p = -\frac{\mu}{K}\mathbf{v}, \tag{3}$$

since these terms scale, respectively, as $\rho f v$ and $\rho v^2 h_0/\lambda^2$, both of which are negligible compared with $\mu v/K$. In equation (3), $\mathbf{v}$, v, p, and K are, respectively, seepage superficial velocity and its magnitude, pore pressure, and bed permeability. For nearly incompressible air, the mass conservation equation

$$\frac{\partial \rho}{\partial t} + \nabla\cdot(\rho\mathbf{v}) = 0 \tag{4}$$

adopts the divergence-free form $\nabla \cdot \mathbf{v} = 0$. With equation (3), the time-averaged pore pressure p then satisfies the Laplace equation

$$\nabla^2 p = 0. \tag{5}$$

However, while a steady pressure p can propagate through the bed according to the elliptic equation (5), *Louge et al.* [2011] showed in their Appendix C that pressure fluctuations p' are attenuated in an isothermal porous medium according to

$$\frac{\partial p'}{\partial t} - \frac{K p_0}{\mu} \nabla^2 p' \simeq 0. \tag{6}$$

In our case, p is close to the ambient atmospheric pressure p_0. A solution of this equation shows that pressure fluctuations of frequency f decay exponentially with distance from the surface on a characteristic "acoustic depth"

$$h_d = \sqrt{\frac{K p_0}{\pi \mu f}}. \tag{7}$$

From equation (7), pressure bursts then induce pore pressure fluctuations down to an acoustic depth $h_d \sim D_d/U$, where $D_d \equiv [100 K p_0/(\pi A_t^2 \rho)]^{1/2}$ has units of a diffusion coefficient. For conditions that we explored, acoustic depths vary from 7 mm at the highest speed to 80 mm at the lowest. Equivalently, at $y \simeq H$, the boxes with $h_0/\lambda = 3\%$ and 6% experienced surface pressure fluctuations up to frequencies $f_d \lesssim 58$ Hz and $\lesssim 35$ Hz, respectively, while faster fluctuations were damped by the porous medium. Conversely, these boxes were brought to the mean static pressure along the free surface in a relatively small time $\sim (2\pi f_d)^{-1} \simeq 3$ ms and $\simeq 5$ ms.

In short, because the Laplace equation (5) is linear, time-averaged pore pressures can be reliably measured within permeable ripples in the wind tunnel. However, pressure fluctuations are naturally low-pass filtered by the porous medium through equation (6).

As *Fourrière et al.* [2010] showed, the time-averaged surface pressure on a sinusoidal ripple with elevation in equation (1) and relatively low h_0/λ evolves along x as

$$p \simeq p_a + p_1 \cos(2\pi x/\lambda + \phi_1), \tag{8}$$

where p_1 scales as $\rho u_*^2 (h_0/\lambda)$ and $\phi_1 < 0$ is a small phase lag that *Kendall* [1970] and *Zilker and Hanratty* [1979] observed in experiments. In equation (8), the base pressure $p_a = p_0 + \tau_{zz}$ arises from a fluctuating turbulent normal stress $\tau_{zz} \simeq \rho u_*^2 \chi^2/3$, where $\chi \sim 3$ is a phenomenological constant [*Fourrière et al.*, 2010].

By imposing equation (8) at the surface and the uniform ambient pressure $p = p_0$ on the ceiling of the box at $y = H$, integrating the Laplace equation (5) yielded the pore "gauge" pressure field

$$p - p_0 = (p_a - p_0)\left(1 - \frac{y}{H}\right) + p_1 \cos(2\pi x/\lambda + \phi_1)\left[\frac{\exp(-2\pi y/\lambda) - \exp(-4\pi H/\lambda)\exp(2\pi y/\lambda)}{1 - \exp(-4\pi H/\lambda)}\right]. \tag{9}$$

Our measurements provided $p - p_0$ at several x and y within the porous ripple. If surface pressure conforms to the single harmonic in equation (8), then equation (9) allowed us to extract $(p_a - p_0)$, p_1, and ϕ_1. Such is the case for the relatively low $h_0/\lambda = 3\%$ in the next section. However, at larger h_0/λ, we will later see that more harmonics are needed.

4. Pore Pressure at Low $h_0/\lambda = 3\%$

To estimate dust penetration into a rippled sand surface conforming to equation (1), *Louge et al.* [2010b] borrowed results from *Gong et al.* [1996], who measured static pressure along a turbulent flow on impermeable smooth and rough wavy surfaces. To calculate pore pressure within a porous sand bed in closed form, they assumed that the data of *Gong et al.* [1996] for a smooth undulating surface conformed to equation (8). In the *Jackson and Hunt* [1975] theory for turbulent flow over slanted terrain, the surface shear stress scales with the aeolian kinetic energy density $\propto \rho U^2$ and roughly with slope, which, for ripples, grows with h_0/λ. Noting that, as a fluid normal stress, static pressure variations on a rippled surface follow the same scaling

10.1002/2014JF003293

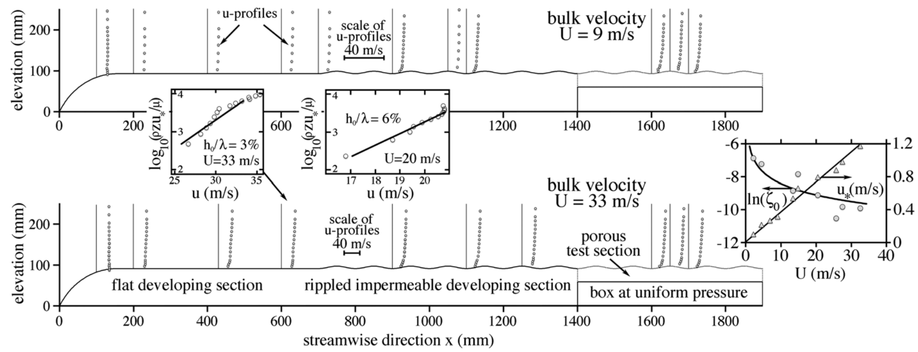

Figure 2. Streamwise evolution of velocity profiles for the rig in Figure 1 at bulk velocities (top) $U \simeq 9$ m/s and (bottom) 33 m/s. Distances are in millimeters. Sections are identified in the bottom graph. Vertical lines are axes $u = 0$, and mark locations where profiles of time-averaged velocity u were recorded. Horizontal segments show a scale of 40 m/s for these profiles. The left inset is a semilog profile of the wall coordinate $\log_{10}(\rho z u_*/\mu)$ versus u at the end of the flat developing section for this facility with $h_0/\lambda = 3\%$ at $U \simeq 33$ m/s. The straight line is a fit to equation (2) yielding aerodynamic roughness ξ_0 and u_* quoted in Table 1 at 95% confidence. The middle inset is for $h_0/\lambda = 6\%$ at $U \simeq 20$ m/s. The right inset shows the overall dependence of $\ln(\zeta_0) \equiv \ln(2\pi\xi_0/\lambda)$ (left axis, dimensionless) and shear velocity u_* (right axis, m/s) on U (m/s) for both rigs at $h_0/\lambda = 3\%$ and 6% over the whole range of bulk velocity considered.

[*Fourrière*, 2009], *Louge et al.* [2010a] suggested that the pressure amplitude measured by *Gong et al.* [1996] could be approximated with the expression

$$p_1 \approx \rho U^2 h_0/(\eta\lambda). \tag{10}$$

(An interpretation of the constant η is that p_1 is the static pressure amplitude that would arise in an ideal steady, incompressible, inviscid, and irrotational flow on a sinusoidal surface located at a distance $\eta\lambda$ below a parallel flat wall.)

The scaling in equation (10) suggests that pressure can be made dimensionless with

$$p^* \equiv \frac{p\lambda}{\rho U^2 h_0}. \tag{11}$$

If this scaling has merit, then the average value of p_1^* over experiments at different wind speeds, denoted by an overbar, should be equal to the inverse of the constant η that *Louge et al.* [2010a] introduced, $\bar{p}_1^* = 1/\eta$.

To gauge whether data for the rippled bed of low amplitude $h_0/\lambda = 3\%$ may be fit with equation (9), we separated variations along the streamwise and depth directions by defining the eigenfunctions

$$g_i(y/\lambda) \equiv \left[\frac{\exp(-2\pi i y/\lambda) - \exp(-4\pi i H/\lambda)\exp(2\pi i y/\lambda)}{1 - \exp(-4\pi i H/\lambda)}\right] \tag{12}$$

and

$$f_i(x/\lambda) \equiv \cos(2\pi i x/\lambda + \phi_i). \tag{13}$$

As Figure 3 shows, pressure data at low h_0/λ are well represented by a single eigenfunction ($i = 1$). Here it is convenient to plot $(p - p_a)/[p_1 g_1(y/\lambda)]$ to highlight variations along the streamwise direction x and $(p - p_a)/[p_1 f_1(x/\lambda)]$ to highlight the corresponding pore pressure decay along the depth y. This approach is equivalent to least squares fitting the 2-D data along (x, y) to equation (9), which represents a truncation of the Fourier series solution of equation (5) to its harmonic fundamental. We found that including higher harmonics for $h_0/\lambda = 3\%$ did not improve the least squares fit, as measured by the adjusted R-squared criterion [*Everitt*, 2006].

Thus, for $h_0/\lambda = 3\%$, we extracted $\eta = 1/\bar{p}_1^* \simeq 0.46 \pm 0.03$ from equation (10). As the dashed line in Figure 3 shows, an extrapolation of our pore pressure measurements to the surface is nearly identical to the pressure data reported by *Kendall* [1970] for an impermeable ripple of comparable wind speed and aspect ratio. Therefore, it appears that permeability similar to a typical sand hardly affects pressure variations on ripple surfaces of low h_0/λ. Later, section 6 will suggest why this is the case.

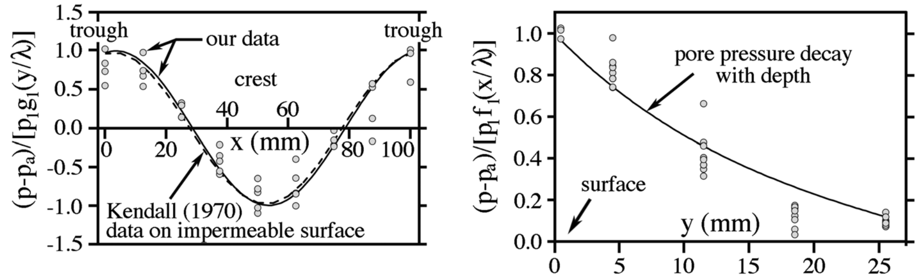

Figure 3. Pressure variations in a porous ripple of amplitude $h_0 = 3$ mm and wavelength $\lambda = 100$ mm swept by wind of bulk speed $U \simeq 9.1$ m/s. (left) Streamwise variations of the relative pore pressure $(p - p_a)/p_1$, divided by the function $g_1(y/\lambda)$ in equation (12) capturing variations in the depth. The dashed line is a fit through comparable data of *Kendall* [1970] for an impermeable surface with similar $h_0/\lambda = 3.125\%$. With $U \simeq 10.6$ m/s, $\zeta_0 \simeq 4.10^{-4}$, and $u_*/U \simeq 0.024$, *Kendall* [1970] found $p_1^* = 1.995 \pm 0.029$ and $\phi_1 = -0.169 \pm 0.015$ at 95% confidence, a result nearly identical to values in Table 1. (right) Variations of relative pore pressure divided by the function $f_1(x/\lambda)$ in equation (13) capturing streamwise variations. Points data and lines are equation (9) with $p_a = 0.37$ Pa, $p_1 = 6.73$ Pa, and $\phi = -0.22$ rad.

Synthesizing data from their own experiments and those of others, *Gong et al.* [1996] had estimated $\eta \simeq 0.14$ and $\simeq 0.51$ for smooth and rough surfaces with $\xi_0 = 30$ μm and 400 μm, respectively. Inspired by those measurements and conscious of the relatively small aerodynamic roughness of desert sands [*Charru et al.*, 2013], *Louge et al.* [2010a] and *Louge et al.* [2010b] adopted the "smooth" value of η that *Gong et al.* [1996] had proposed. However, as the next section shows, this choice was not wise, largely because *Gong et al.* [1996] conducted their measurements on ripples with higher aspect ratio, which are more likely to induce flow separation. Thus, our results show that *Louge et al.* [2010b] overestimated pore pressure amplitudes by a factor $\simeq$ 3 and seepage-induced dust capture and moisture channeling by the same factor. Nonetheless, this mechanism of dust capture remains significant and is now quantified.

Our data also show that like over impermeable walls, surface pressure on a porous sinusoidal bed at $h_0/\lambda = 3\%$ (equation (1), with y pointing downward) is sinusoidal with a slight phase lag. *Kuzan et al.* [1989] drew a phase diagram delimiting regimes of attached and separated flows over impermeable sine waves (Figure 4). At the wind speeds of our experiments, this map suggests that flows are attached to the surface with $h_0/\lambda = 3\%$, except perhaps for the two smallest speeds that we staged, shown as the rightmost two diamond symbols in Figure 4 with $U \simeq 4.4$ and 9.1 m/s. In fact, Figure 3 hints that such flow separation might have indeed occurred at $U \simeq 9.1$ m/s. For an attached turbulent boundary layer, pressure fluctuations are approximately $p' \sim 3\rho u_*^2$ [*Hinze*, 1975]. Thus, relative to p_1, they are $p'/p_1 \sim (3A_t^2/\bar{p}_1^*)(\lambda/h_0)$, where $A_t \equiv u_*/U \simeq 0.04$ and $\bar{p}_1^* \simeq 2$ (Table 1) or $p'/p_1 \simeq 8\%$. There are regions along the ripple where pressure deviations exceed this estimate, particularly just after the crest ($x \simeq 60$ mm).

Because pressure amplitude scales with h_0/λ, ripples of lower aspect ratio (i.e., ripple index > 17) should also exhibit a similar, slightly delayed sinusoidal surface pressure, and their flow should be even less likely to separate. In contrast, as h_0/λ grows (i.e., for lower ripple index), Figure 4 suggests that the flow is more prone to detachment, and therefore, our measurements at low aspect ratio are no longer sufficient to expose how the porous subsurface affects the turbulent flow. In fact, static pressure variations along the impermeable sinusoidal surface of *Gong et al.* [1996] with $h_0/\lambda \simeq 7.9\%$ did not, strictly speaking, conform to the harmonic equation (8). Conscious of this shortcoming, we therefore staged a larger $h_0/\lambda = 6\%$ for comparison, as discussed next.

5. Pore Pressure at $h_0/\lambda = 6\%$

Because turbulent flows over waves of large amplitude separate [*Kuzan et al.*, 1989], we could no longer model pore pressure within artificial ripples of $h_0/\lambda = 6\%$ with a single harmonic. Instead, we found it necessary to interpret data using a longer series of eigenfunctions satisfying the boundary condition at $y = H$. We truncated the series to the third harmonic, beyond which we observed no further improvement in the R-squared criterion that gauges confidence in the best fit,

$$p - p_0 = (p_a - p_0)\left(1 - \frac{y}{H}\right) + \sum_{i=1}^{3} p_i f_i(x/\lambda) g_i(y/\lambda) + p_d f_{1/n}(x/\lambda) g_{1/n}(y/\lambda). \quad (14)$$

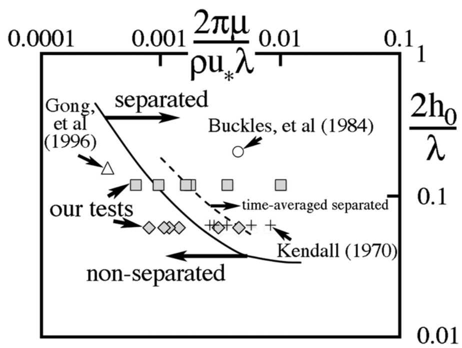

Figure 4. Regime map proposed by *Kuzan et al.* [1989] for turbulent flows over sinusoidal impermeable ripples [*Frederick and Hanratty*, 1988]. Solid lines delimit regions in the diagram of inverted Reynolds number $2\pi\mu/(\rho u_*\lambda)$ versus ripple aspect ratio $2h_0/\lambda$, behaving as "separated" or "nonseparated" flows [*Thorsness et al.*, 1978]. To the right of the dashed line, *Kuzan et al.* [1989] noted a transition to "time-averaged separated" flows remaining detached on longer time scales. The solid triangle marks experiments of *Gong et al.* [1996]; the circle shows experiments of *Buckles et al.* [1984], which *Henn and Sykes* [1999] modeled with LES; plus signs are experiments of *Kendall* [1970]; and solid diamonds and squares indicate our own tests with $h_0/\lambda = 3\%$ and 6%, respectively.

To this series, we added the last term $p_d f_{1/n} g_{1/n}$ representing the relatively small decay in mean static pressure that wind experiences on length scales $\gg \lambda$ as it drags the rippled surface. For compatibility with the Laplace equation (5), this "drag" term is a single slowly varying subharmonic eigenfunction valid in the range $0 < x < \lambda$ of the form $f_{1/n}(x/\lambda) \equiv \cos[2\pi x/n\lambda + \phi_d]$ and $g_{1/n}(y/\lambda) \equiv [\exp(-2\pi y/n\lambda) - \exp(-4\pi H/n\lambda)\exp(2\pi y/n\lambda)]/[1 - \exp(-4\pi H/n\lambda)]$, which we obtain by substituting $i = 1/n$ in equations (12) and (13). Because such drag-induced pressure reduction is small, the actual form of the subharmonic term $p_d f_{1/n} g_{1/n}$ matters little to our results. Values of n and p_d are found in Table 1.

As Figure 4 shows, the more complicated form of pore pressure in equation (14) is consistent with the regime map that *Kuzan et al.* [1989] drew for harmonically rippled impermeable surfaces. This map implies that most of our tests at $h_0/\lambda = 6\%$ separated behind crests, while those at $h_0/\lambda = 3\%$ did not. Despite a lower value of inverted Reynolds number $2\pi\mu/(\rho u_*\lambda)$, the experiments of *Gong et al.* [1996] at $h_0/\lambda \simeq 7.9\%$ should not have separated either, according to this map. However, as Figure 5 illustrates, surface pressures of *Gong et al.* [1996] closely resemble those of *Buckles et al.* [1984] and *Henn and Sykes* [1999], suggesting that they too exhibited separated flow.

Further evidence of flow recirculation behind crests is the relatively low pressure recorded on impermeable surfaces in the range $0.7 \lesssim x/\lambda \lesssim 1$ and the delayed location of peak pressure. Unlike surface pressure profiles at $h_0/\lambda = 3\%$ (Figure 3, left, with $y \sim 0$), peak pressures at larger h_0/λ in Figure 5 are not located above troughs, but they are delayed to $x/\lambda \sim 0.25$ for impermeable surfaces (symbols) or to $x/\lambda \sim 0.16$ over our porous bed (solid line).

Finally, by comparing pressure data from wavy surfaces with different values of h_0/λ, Figure 5 confirms that like shear stress or u_*^2 [*Jackson and Hunt*, 1975], pressure scales with h_0/λ. However, as the inset of Figure 5 reveals, there is a subtle dependence of the principal pressure harmonic p_1^* from equation (14) on wind speed.

More significantly, our extrapolation of pore pressure to the surface (solid line in Figure 5) clearly deviates from similar measurements on impermeable surfaces. In the next section, we suggest why these deviations can be attributed to the porous medium.

6. Significance for Turbulent Flows Over Porous Rippled Surfaces

Besides closely capturing pore pressure within the rippled bed, equation (14) provides an accurate record of static pressure on its surface, shown as the solid line in Figure 5. Using a Monte Carlo technique, we calculated where this line resides at 95% confidence. As Figure 5 reveals, the dimensionless surface pressure at the porous crest with $h_0/\lambda = 6\%$ is identical within experimental errors to earlier measurements [*Buckles et al.*, 1984; *Gong et al.*, 1996] and numerical simulations [*Henn and Sykes*, 1999] on impermeable wavy surfaces of similar aspect ratios, thus validating our measurements and suggesting that the scaling of pressure in equation (11) is robust. However, we find that surface pressure and its gradient in the region $0.1 \lesssim x/\lambda \lesssim 0.45$ between trough and crest are substantially lower on the porous ripple than they are on a similar impermeable surface.

This contrast between pressure profiles on impermeable and porous wavy surfaces suggests that the porous medium interferes with the turbulent flow overhead. At a porous surface of upward unit normal $\hat{\mathbf{n}}$, *Beavers and Joseph* [1967] recorded a substantial slip velocity $\mathbf{u}_s$, which they related to the superficial velocity $\mathbf{v}$ in the bed through a boundary condition that *Jones* [1973] later interpreted in terms of the surface shear stress $\boldsymbol{\tau}$ [*Nield*, 2009]. In a clear-gas turbulent viscous sublayer, this condition writes

$$\boldsymbol{\tau} \cdot \hat{\mathbf{n}} = \frac{\varpi \mu}{K^{1/2}} \left(\mathbf{u}_s - \mathbf{v} \right), \tag{15}$$

where ϖ is a constant of order unity. (As *Saffman* [1971] pointed out, the superficial velocity of order K is small compared with the slip of order $K^{1/2}$, and thus, it can be neglected.)

Meanwhile, as *Durán et al.* [2011] explained, the "outer layer" far above a rippled surface of moderate h_0/λ behaves as a nearly inviscid potential flow having streamlines in phase with ripple elevation and a peak velocity located above crests. Closer to the surface, Reynolds stresses in the turbulent "inner layer" delay the response of fluid velocity to an imposed shear, thus compelling wall shear stress to peak ahead of crests and pressure maxima to lag behind troughs. *Fourrière et al.* [2010] showed that the inner layer thickness ℓ satisfies $\ell/\lambda \sim \ln^{-2}(\ell/\xi_0)$. Closer to the surface, the viscous sublayer defines the aerodynamic roughness ξ_0 that the inner layer experiences. As long as the thickness of the viscous sublayer $\ell_v \simeq 5\mu/(\rho u_*)$ is small compared to that of the inner layer, then details of how aerodynamic roughness arises do not matter to the evolution of shear stress and pressure along the ripple. For our conditions, $1.5 < \ell < 3.1$ mm is substantially larger than $59 < \ell_v < 400$ µm but much smaller than λ, therefore validating the assumptions underlying the analysis of *Fourrière et al.* [2010].

With these assumptions, *Kroy et al.* [2002] extended the theory of *Jackson and Hunt* [1975] for turbulent flows over topography to dunes and ripples. They showed that shear stress on a sinusoidal surface of moderate h_0/λ evolves as

$$\tau = \rho u_*^2 (1 - \hat{\tau}), \tag{16}$$

where $\phi_\tau = \arctan(B/A)$ and

$$\hat{\tau} \equiv 2\pi \left(\frac{h_0}{\lambda} \right) (A^2 + B^2)^{1/2} \cos \left(2\pi \frac{x}{\lambda} + \phi_\tau \right) \tag{17}$$

is a dimensionless excursion in shear stress. To a good approximation, *Fourrière et al.* [2010] calculated

$$A \simeq 2 + \frac{a_1 + a_2 R + a_3 R^2 + a_4 R^3}{1 + a_5 R^2 + a_6 R^4} > 0, \tag{18}$$

$$B \simeq \frac{b_1 + b_2 R + b_3 R^2 + b_4 R^3}{1 + b_5 R^2 + b_6 R^4} > 0, \tag{19}$$

where $a_i \simeq (1.070, 0.0931, 0.108, 0.0248, 0.0416, 0.00106)$ and $b_i \simeq (0.0370, 0.158, 0.115, 0.00202, 0.00287, 0.000535)$. The dimensionless constants A and B are weakly related to the aerodynamic roughness ξ_0 through

$$R \equiv -\ln \left(\frac{\xi_0}{\lambda} \right) > 0. \tag{20}$$

Combining equation (15) with $v \simeq 0$ and equation (16), the ratio of slip to shear velocity is then

$$\frac{u_s}{u_*} \simeq \mathrm{Re}_K (1 - \hat{\tau}) / \varpi \tag{21}$$

where $\mathrm{Re}_K \equiv \rho u_* \sqrt{K}/\mu$. If for simplicity we assume that at low h_0/λ, Prandtl's logarithmic law applies to the inner layer then the velocity profile becomes $u = (u_*/\kappa)\ln(z/\xi_0) + u_s$ or, equivalently, $u = (u_*/\kappa)\ln(z/\xi_s)$, where ξ_s is an effective "slip roughness" that varies along the surface,

$$\xi_s \equiv \xi_0 \exp \left(-\frac{u_s \kappa}{u_*} \right) = \xi_0 \exp \left[-\frac{\kappa}{\varpi} \mathrm{Re}_K (1 - \hat{\tau}) \right]. \tag{22}$$

At low enough h_0/λ, $\hat{\tau} < 1$ so that the slip roughness ξ_s decreases everywhere sharply with wind speed.

As *Manes et al.* [2009, 2011] showed for flat beds of much higher permeability ($K \simeq 10^{-8} - 10^{-7}$ m^2), turbulence can also penetrate a permeable porous substrate, thus further perturbing the turbulent boundary layer, for example, by reducing the apparent von Kármán constant κ as Re_K grows. However, the data of *Manes et al.* [2009, 2011] imply that these more dramatic effects disappear at the lower permeabilities typical of desert sands, where Re_K remains small.

Nonetheless, equation (21) suggests that a significant slip velocity can arise on a porous rippled surface. For example, with typical $A \simeq 4$ and $B \simeq 2$ at $u_* = 0.3$ m/s, equations (17) and (21) predict that our porous rig with $h_0/\lambda = 6\%$ and $K = 3.4\ 10^{-11}$ m^2 can produce a peak slip $u_s/u_* \simeq 0.3$ that is a notable fraction of the shear velocity. Meanwhile, for the same conditions, the slip is much smaller on a flat surface ($h_0/\lambda = 0$), $u_s/u_* \simeq 0.1$. The form of equation (21) suggests that the rippled nature of the porous surface begins to produce a significant slip when the amplitude of $\hat{\tau}$ in equation (17) exceeds 1 or, equivalently, for aspect ratios $h_0/\lambda > 1/[2\pi(A^2 + B^2)^{1/2}]$. With typical values $A \simeq 4$ and $B \simeq 2$ [*Fourrière et al.*, 2010], this occurs with $h_0/\lambda \gtrsim 4\%$, suggesting that the shallow ripples in section 4 possess a nearly uniform slip roughness $\xi_s \sim \xi_0 \exp\left(-\kappa \mathrm{Re}_K/\varpi\right)$. However, as h_0/λ grows to 6%, the slip should vary significantly anywhere along the ripple, unless surface shear stress collapses through flow separation.

In other words, as far as surface pressure is concerned, a porous ripple at $h_0/\lambda = 3\%$ should behave as an impermeable ripple with uniform, albeit smaller aerodynamic "slip" roughness. However, for greater h_0/λ, the slip roughness should evolve along porous ripples, thus modifying the character of the turbulent boundary layer.

Nonetheless, the reduction in slip roughness with u_* that is predicted by equation (22) seems at odds with the results of *Gong et al.* [1996]. At relatively large values of $h_0/\lambda = 7.9\%$, these authors observed a *larger* pressure amplitude on a *smooth* impermeable sinusoidal surface with $\xi_0 = 30$ μm than on a rougher surface with $\xi_0 = 400$ μm. Meanwhile, our plastic surfaces with $h_0/\lambda = 6\%$ have an aerodynamic roughness $0.4 < \xi_0 < 11$μm comparable to the smooth case of *Gong et al.* [1996]. (Moreover, as equation (22) suggests, our porous ripples should produce an even smaller effective roughness by allowing slip at the wall.) Therefore, based upon trends that *Gong et al.* [1996] observed for the variations of pressure amplitude with aerodynamic roughness, our smoother porous ripples with $h_0/\lambda = 6\%$ should have produced a larger dimensionless pressure amplitude p^* than what *Gong et al.* [1996], *Buckles et al.* [1984], or *Henn and Sykes* [1999] measured on impermeable ripples. Yet the opposite happened: as Figure 5 shows, surface pressure variations declined from impermeable to porous ripples; further, as the inset of that figure shows, the first pressure harmonic p_1^* decreased with wind speed.

Therefore, another mechanism that is absent from impermeable experiments must be at play when h_0/λ is relatively large. Our observations suggest that porous ripples allow air to bypass the main flow. Because pore pressure satisfies the elliptic Laplace equation (5), the depression at the crest diffuses through the porous bed, thus substantially reducing surface pressure upstream. (Less noticeably, the depression also permeates leeward, producing a lower surface pressure in the range $0.6 \lesssim x/\lambda \lesssim 1$ than the corresponding value on an impermeable surface.) Our measurements suggest that it does not take much air seepage to create an internal bypass attenuating the peak pressure through such retrodiffusion of the depression on the crest. An attenuation Δp^* across the dimensionless distance Δx^* requires a seepage velocity v given by equation (3) as

$$\frac{v}{U} \sim \left(\frac{\Delta p^*}{\Delta x^*}\right)\left(\frac{\rho K^{1/2} U}{\mu}\right)\left(\frac{h_0}{\lambda}\right)\left(\frac{K^{1/2}}{\lambda}\right) \tag{23}$$

For example, as Figure 5 shows, the drop $\Delta p^* \simeq 1.2$ across $\Delta x^* \simeq 0.25$ from peak pressure at $x^* \simeq 0.25$ to crest depression at $x^* \simeq 0.5$ only requires a seepage velocity as small as $v \simeq 0.5$ mm/s for $U = 10$ m/s. However, because seepage velocity scales as $K^{1/2}/\lambda$ in equation (23), an internal bypass that can attenuate surface pressure on the ripple scale is not important on the size of a dune, which has vanishingly small $K^{1/2}/\lambda$.

Because the principal ingredient in the theory of *Jackson and Hunt* [1975] is local slope, represented in our sinusoidal case by h_0/λ, we expect that any porous bed with similar size and slope, such as triangular aeolian ripples [*Tanner*, 1967], will create comparable slip roughness and attenuate surface pressure gradients in ways that are analogous to a sinusoidal profile. The recent experiments of *Blois et al.* [2014] confirm this with coarse gravel beds. In their case, particles are so large that permeability is high, thus creating a visible fluid bypass through the bed.

10.1002/2014JF003293

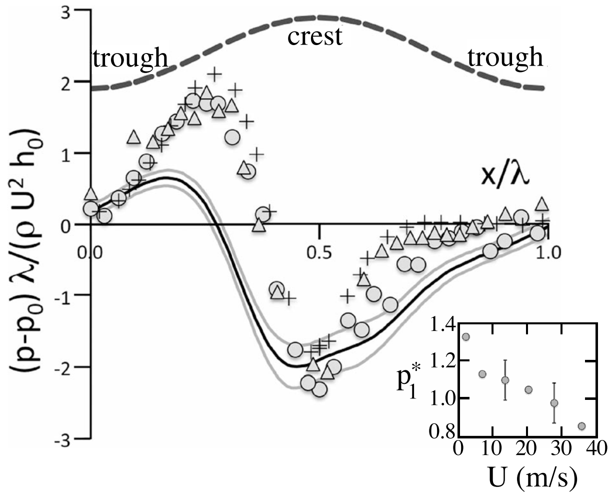

Figure 5. Comparison of static pressure on impermeable and porous surfaces. Symbols mark measurements on impermeable solids by, respectively, *Buckles et al.* [1984] (circles) and *Gong et al.* [1996] (triangles, their rough surface) and computed in large eddy simulations labeled "BHA1" by *Henn and Sykes* [1999] (plus signs). The solid line is an extrapolation of measurements within our porous bed with $h_0/\lambda = 6\%$ to the surface using equation (14) (solid line), based on parameters in Table 1. Grey lines demarcate our 95% confidence interval. The abscissa is x/λ with origin over the trough; the ordinate is $(p^* - p_0^*)$. The upper sketch (exaggerated amplitude) shows positions of trough and crest. The inset shows variations of the main harmonic in equation (14) versus U with error bar from Table 1.

Because by necessity our experiments were run without particles, they only applied, strictly speaking, to winds below the suspension threshold. However, we anticipate that our artificial rippled surfaces capture effects of porosity on surface slip and streamwise wind pressure gradient, whether or not the wind is laden with particles, for three reasons. First, our porous plastic has comparable $\sqrt{K} \simeq 5.8\,\mu\text{m}$ to a typical sand bed ($\sqrt{K} \simeq 2\,\mu\text{m}$). Second, because ripples travel at a speed $\ll u_*$, seepage is established much faster than ripple shape changes. Third, as *Bagnold* [1942] noted, the momentum exchange between air and suspended solids binds altitude z_B and speed u_B at the top of the saltation layer. (For this reason, z_B is called the "Bagnold focal point.") Therefore, consistent with Prandtl's law of the wall, the particle-laden region presents to the turbulent inner layer aloft an effective aerodynamic roughness [*Durán et al.*, 2011]

$$\xi_B \equiv z_B \exp\left(-\frac{u_B \kappa}{u_*}\right). \tag{24}$$

As *Sherman and Farrell* [2008] reviewed, $g\xi_B/u_{*\text{th}}^2$ grows with shear velocity above the transport threshold $u_{*\text{th}}$ (in contrast with the slip roughness ξ_s that we introduced in equation (22), which instead decreases with wind speed). Because the coefficients in equations (18)–(20) depend logarithmically on ξ_s, they change slowly. Meanwhile, to predict the streamwise evolution of surface pressure, *Fourrière* [2009] derived other coefficients (called C and D) with similarly weak logarithmic dependence on roughness. Therefore, we expect that pore pressure evolution is qualitatively similar with or without sand transport, as *Fourrière et al.* [2010] noted for shear stress. However, because the theory of *Jackson and Hunt* [1975] is predicated upon an inner layer that is thicker than the viscous sublayer, a saltation region with $z_B \sim u_{*\text{th}}^2/g$ may become too thick to uphold the theory's principal assumption, and therefore, it might no longer produce quantitative predictions of shear stress and pressure. In addition, because particles near the surface affect the suspension viscosity [*Mooney*, 1951], the clear-gas boundary condition in equation (15) should be changed accordingly, and τ should be replaced by the gas contribution to the total stress. Nonetheless, our experiments provide a first insight toward appreciating the role of bed porosity on aeolian rippled surface processes in deserts.

7. Pressure Drag and Lift

At the wavy surface with unit normal of components $[2\pi h_0^* \sin(2\pi x^*); 1]/\left[1 + 4\pi^2 h_0^{*2} \sin^2(2\pi x^*)\right]^{1/2}$ along x and y, pressure integrates to a force $\mathbf{P}$ exerted on a unit ripple width over the whole wavelength. Its projection along the flow amounts to a pressure drag force per unit width, expressed in dimensionless form as

$$P_x^* \equiv \frac{1}{\lambda}\frac{\mathbf{P}\cdot\hat{\mathbf{x}}}{\rho U^2}\left(\frac{\lambda}{h_0}\right) = \int_0^1 (p^* - p_0^*)\frac{2\pi h_0^* \sin(2\pi x^*)}{\left[1 + 4\pi^2 h_0^{*2} \sin^2(2\pi x^*)\right]^{1/2}}\mathrm{d}x^*, \tag{25}$$

while its projection along y resembles a lift

$$P_y^* \equiv \frac{1}{\lambda}\frac{\mathbf{P}\cdot\hat{\mathbf{y}}}{\rho U^2}\left(\frac{\lambda}{h_0}\right) = \int_0^1 (p^* - p_0^*)\frac{\mathrm{d}x^*}{\left[1 + 4\pi^2 h_0^{*2} \sin^2(2\pi x^*)\right]^{1/2}}. \tag{26}$$

In these expressions, distances are made dimensionless with λ and denoted by an asterisk. As Table 1 shows, the dimensionless net pressure drag force grows roughly in proportion to h_0/λ, thus suggesting that

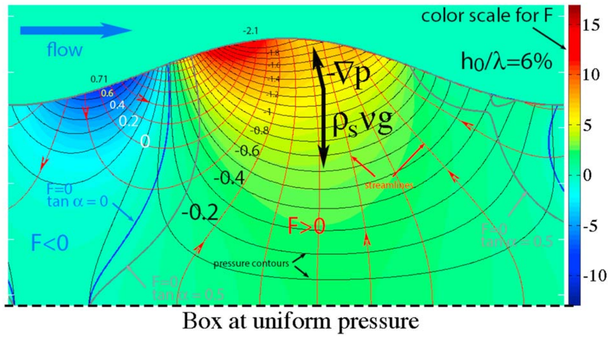

Figure 6. Contours of seepage streamlines and dimensionless gauge pore pressure $p^* - p_0^*$ across a section of the porous ripple with $h_0/\lambda = 6\%$, bounded on top by the harmonic ripple described in equation (1) and by a hermetic box with pressure p_a at $y = H = 42$ mm below. Figure is drawn to scale. Numerical values are reconstructed from equation (14) with dimensionless constants in Table 1. Red and black lines are, respectively, streamlines and contours of $p^* - p_0^*$ with values in the range $-2.1 < p^* - p_0^* < 0.71$. For a frictionless bed ($\tan\alpha = 0$), colors represent the magnitude of F in equation (30) with $-8.7 < F < 15.1$ and thick blue lines mark the locus of $F = 0$. The maximum $F_{max} = 15.1$ is ahead of the crest at $x/\lambda \simeq 0.40$. Thick grey lines are the same locus for $\tan\alpha = 0.5$. Note that because the term $\propto p_d$ in equation (14) dissipates pressure slightly from $x = 0$ to $x = \lambda$, patterns are aperiodic along x. Black arrows illustrate typical body forces exerted on a point within the porous ripple (not to scale). In this sketch, the opposite of the pore pressure gradient $-\nabla p$ is not aligned with the gravitational body force $\rho_s \nu g$, but it contributes to relieving it.

$\mathbf{P} \cdot \hat{\mathbf{x}} \propto \rho U^2 h_0^2/\lambda$. It is significantly smaller than the same quantities derived from the surface pressure data of *Gong et al.* [1996] (smooth surface, $P_x^* \simeq 0.25$, and "rough" surface, $P_x^* \simeq 0.18$ at $h_0/\lambda \simeq 7.9\%$), *Buckles et al.* [1984] ($P_x^* \simeq 0.24$ at $h_0/\lambda \simeq 10\%$), and from the large eddy simulation (LES) of *Henn and Sykes* [1999] ($P_x^* \simeq 0.22$ at $h_0/\lambda \simeq 10\%$), confirming that air seepage through the porous medium reduces pressure drag on the ripple surface.

Our experiments also yielded $P_y^* < 0$, indicating that the ripple surface was subject to an upward lift. Comparison of $|P_y^*|$ for ripples with $h_0/\lambda = 6\%$ and 3% in Table 1 suggests that $|P_y^*| \propto h_0^{*2}$, tentatively suggesting a lift force $\mathbf{P} \cdot \hat{\mathbf{y}} \propto \rho U^2 h_0^3/\lambda^2$. In contrast, earlier experiments over impermeable wavy surfaces could be of either sign; the rough surface of *Gong et al.* [1996] had $P_y^* \simeq 0.10$; their smooth one had $P_y^* \simeq -0.28$; *Buckles et al.* [1984] had $P_y^* \simeq -0.15$, but the corresponding LES found $P_y^* \simeq +0.14$ [*Henn and Sykes*, 1999].

Finally, as Table 1 shows, we noted that ripples of relatively large aspect ratio induce a net seepage updraft. Making superficial velocity v dimensionless as $v^* \equiv v[\mu\lambda^2/(K\rho U^2 h_0)]$, the net seepage (positive downward) calculated at $y = H$ is

$$v^* = -\int_0^1 \hat{\mathbf{y}} \cdot \nabla^* p^* \mathrm{d}x^*. \tag{27}$$

The mean updraft at $h_0/\lambda = 6\%$ suggests that porous ripples of high aspect ratio exhale a net amount of pore air as wind blows over their surface. At lower $h_0/\lambda = 3\%$, the draft is smaller and directed downward instead.

8. Body Forces

We derive isobaric contours and seepage streamlines within the ripple from the two-dimensional fit of the pore pressure field in equation (14). They are sketched in Figures 6 and 7. (All original mean pore pressure data leading to these fits are found in the supporting information.) As *Louge et al.* [2010a] calculated in their Appendix A, the pore pressure gradient within a homogeneous porous sand bed exerts an equal and opposite body force $-\nabla p$ on the grain assembly. A frictionless bed with solid volume fraction ν and grains of material density ρ_s would therefore mobilize if the downward projection of this gradient $\hat{y} \cdot \nabla p$ balanced the gravitational body force $\rho_s \nu g$. If instead the bed failed as a Mohr-Coulomb material with internal friction, which nearly equals the tangent of the angle of repose α, then its local force balance would also involve the component of the gradient along $\hat{\mathbf{x}}$ [*Louge et al.*, 2010a]. In this case, grain mobilization would take place wherever

$$\frac{\partial p}{\partial y} - \tan\alpha \left|\frac{\partial p}{\partial x}\right| \geqslant \rho_s \nu g. \tag{28}$$

In criterion (28), the absolute value indicates that internal friction hinders the onset of mobilization by redirecting the body force $\partial p/\partial x$ to the downward vertical direction, whatever its sign. *Tsinontides and Jackson* [1993] and *Loezos et al.* [2002] elucidated a similar effect in gas-solid fluidized beds.

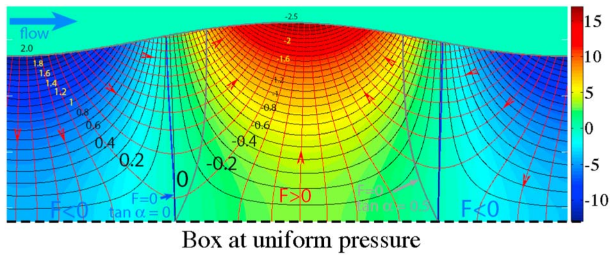

Figure 7. Cross section of the porous ripple with $h_0 / \lambda = 6\%$ and $H = 32.5$ mm. Figure is drawn to scale. For the meaning of lines and color scale, see Figure 6. Note the greater symmetry at this smaller aspect ratio. Ranges of $p^* - p_0^*$ and F are provided in Table 1. The maximum $F_{max} = 16.7$ is behind the crest at $x/\lambda \simeq 0.53$.

When sand ripples are buffeted by a strong wind, a pore pressure gradient directed downward can also relieve a substantial part of the bed weight below them, even without complete grain mobilization. On parts of the sand-free surface where such downward gradient exists, the corresponding force can thus facilitate the onset of erosion. This contribution of pore pressure gradients is generally ignored, whereby grain ejection is thought to occur after u_* reaches a certain threshold, and subsequent erosion is entirely attributed to surface shear [*Shields*, 1936; *Shao and Lu*, 2000]. Nonetheless, recent studies have shown that certain geophysical flow over a porous bed can develop static pressures below the mean ambient value, thus creating pore pressure gradients below the surface that affect flow dynamics [*Iverson*, 2005; *Roche et al.*, 2010; *Iverson et al.*, 2011; *Louge et al.*, 2011; *Carroll et al.*, 2013].

In this section, we exploit our measurements to calculate the propensity of harmonic ripples to relieve gravity. From criterion (28), this is measured with the ratio

$$\mathbb{F} \equiv \frac{\partial p/\partial y - \tan\alpha |\partial p/\partial x|}{\rho_s \nu g}; \tag{29}$$

if $\mathbb{F} \geqslant 1$, then the bed is mobilized; if $0 < \mathbb{F} < 1$, gravity is partially relieved by pore pressure gradients, possibly leading to bed expansion [*Louge et al.*, 2010a]; if $\mathbb{F} < 0$, gravity is augmented by the gradients, perhaps contributing to bed compaction. To cast our results in more general terms, we define

$$F \equiv \frac{\partial p^*}{\partial y^*} - \tan\alpha \left| \frac{\partial p^*}{\partial x^*} \right|, \tag{30}$$

where distance is made dimensionless with wavelength, $(x^*, y^*) \equiv (x, y)/\lambda$, and p^* is given by equation (11). Then, the ratio in equation (29) becomes $\mathbb{F} = \mathbb{R}F$, where the dimensionless group

$$\mathbb{R} \equiv \frac{\rho U^2 h_0}{\rho_s \nu g \lambda^2} \tag{31}$$

has the structure of a Sleath number [*Sleath*, 1999] and represents how wind kinetic energy counteracts the gravitational pull on a rippled sand bed. *Louge et al.* [2010a] introduced a similar dimensionless number governing rapid snow eruption as the front of a powder avalanche passes over a porous snow pack.

Equations (29)–(31) imply that because $\mathbb{R}$ depends linearly on ripple amplitude but quadratically on wavelength, longer ripples are less susceptible to pore pressure gradients than smaller ones at a constant aspect ratio h_0/λ. If the flow did not separate behind crests at large aspect ratios h_0/λ, then we would expect F to remain roughly independent of wind speed, sand density, gravitational acceleration, ripple amplitude, or wavelength, while the role of these quantities would be captured by $\mathbb{R}$. This is essentially what *Gong et al.* [1996] suggested with the scaling in equation (10).

To gauge to what extent ripple aspect ratio matters, Figures 6 and 7 contrast the distribution of F for $h_0/\lambda = 6\%$ and 3%. Here we calculate F by substituting average pressure coefficients ($\bar{p}_i^*$, $\bar{p}_a^*$, $\bar{p}_d^*$), phases ($\bar{\phi}_i$, ϕ_d), and index n from Table 1 in equation (14) and differentiating. As expected, F spans similar magnitudes for both aspect ratios (Table 1). If friction is introduced, the domain where pressure gradients relieve gravity ($F > 0$) becomes narrower. Although the maximum value of F decreases with increasing $\tan\alpha$, this reduction is small. For $\tan\alpha = 0.5$, $F_{max} = 16.5$ at $h^* = 3\%$ and $F_{max} = 13.8$ at $h^* = 6\%$.

Crucially, we find that while porous ripples of low aspect ratio maintain a relatively symmetric seepage flow pattern (Figure 7), ripples of a greater h_0/λ possess a pressure field that is significantly skewed toward the upstream face (Figure 6). Coincidentally, the greatest propensity for seepage to relieve gravity (i.e., where F peaks at F_{max}) lies approximately ($\lambda/10$) ahead of the crest, where the theory of *Jackson and Hunt* [1975] also locates maximum shear stress. Thus, if ripples exhibit a large aspect ratio, it is possible for wind-induced grain mobilization to augment shear-induced erosion there.

To compare the relative importance of the two effects, we invoke the correlation of *Shao and Lu* [2000] for the onset of aeolian transport at a threshold shear velocity $u_{*\mathrm{th}}$. For cohesionless surface grains of diameter d, they wrote $\rho u_{*\mathrm{th}}^2 \simeq A_N \rho_s g d$, where $A_N \simeq 0.0123$ is an empirical constant inspired by insights of *Bagnold* [1935] and *Shields* [1936]. For a typical turbulent boundary layer, the shear velocity u_* is related to U through $u_* = A_t U$. (Table 1 has $A_t \simeq 3.7\%$ and 3.8% for $h_0/\lambda = 3\%$ and 6%, respectively.) Therefore, $u_{*\mathrm{th}}$ can be converted to a threshold U_{Shields} in bulk wind speed,

$$\rho U_{\mathrm{Shields}}^2 \simeq \frac{A_N}{A_t^2} \rho_s g d. \tag{32}$$

Meanwhile, grain mobilization by pore pressure gradients arises first where $F\mathbb{R} = 1$, i.e., where F is largest. Therefore, substituting equation (31), such incipient mobilization occurs past a minimum wind energy

$$\rho U_\Delta^2 = \frac{\rho_s g \nu \lambda^2}{F_{\max} h_0}. \tag{33}$$

Note that this prediction of a threshold speed U_Δ independent of particle diameter is in sharp contrast with traditional gas-solid fluidized beds, in which the superficial gas velocity v_{mf} at minimum fluidization increases with particle size. As *Tsinontides and Jackson* [1993] showed, a frictionless bed fluidizes as soon as v reaches v_{mf}, thus adopting the gravity-driven pressure gradient $\nabla p = \rho_s \nu \mathbf{g}$ so that $v_{\mathrm{mf}} = K \rho_s \nu g/\mu$; because $K \simeq d^2(1-\nu)^3/(150\nu^2)$, then $v_{\mathrm{mf}} \propto d^2$. The chief reason for interpreting differently the onsets of gas-solid fluidization and grain mobilization by pore pressure gradients is that the former must impose a *superficial gas velocity* $> v_{\mathrm{mf}} \propto d^2$, while the latter reaches a wind-driven *pore pressure gradient* $> \rho_s \nu g$ through an equation (5) that is independent of K and therefore of d. *Sleath* [1999] and *Foster et al.* [2006] described a mechanism for oscillatory flows over sediment beds that are independent of d for a similar reason.

Comparing equations (32) and (33), we predict that as wind speed increases, grain mobilization by deep pore pressure gradients takes place before Shields erosion of surface grains whenever $U_\Delta < U_{\mathrm{Shields}}$ or, equivalently, when

$$\frac{\sqrt{h_0 d}}{\lambda} > \sqrt{\frac{A_t^2 \nu}{A_N F_{\max}}}. \tag{34}$$

With $A_N \simeq 0.0123$ [*Shao and Lu*, 2000], $\nu \simeq 0.6$ for a typical sand bed, $A_t \simeq 0.03$, and $F_{\max} \simeq 15$ (Table 1), the constant on the right of equation (34) is $\simeq 0.054$. Thus, for typical desert ripples with $h_0 \simeq 4$ mm, $\lambda \simeq 10$ cm, and $d \simeq 350$ µm [*Andreotti et al.*, 2006], pressure gradient-induced grain mobilization should not contribute significantly to overall erosion. However, if such ripples of small aspect ratio became armored by millimetric surface grains of diameter d immobilizing smaller particles below [*Manukyan and Prigozhin*, 2009], then $\sqrt{h_0 d}/\lambda$ could rise to values approaching criterion (34). With such armoring, ripples should then naturally restructure into longer wavelengths to bring down $\sqrt{h_0 d}/\lambda$, lest their foundation of smaller particles disappeared under the action of pore pressure gradients. Such behavior might be relevant to the formation of "megaripples," which feature a large aspect ratio $h_0/\lambda > 3\%$, as well as coarse surface grains able to withstand greater shear velocity before being entrained themselves [*Yizhaq et al.*, 2012].

9. Summary and Conclusions

We measured pore pressure below two sinusoidal surfaces of wavelength $\lambda = 100$ mm and amplitude $h_0 = 3$ mm and 6 mm subject to turbulent flows of bulk speed $3 < U < 36$ m/s in the wind tunnel. The resulting aspect ratios $h_0/\lambda = 3\%$ and 6% straddled a wide range of ripple index RI observed in the field [*Tanner*, 1967]. However, to permit comparisons with existing literature on impermeable wavy surfaces, we focused attention on sinusoidal ripples, ignoring for now the asymmetry of desert ripples.

Pore pressure at the smallest aspect ratio $h_0/\lambda = 3\%$ was a single harmonic function of streamwise distance lagging the crest slightly and decaying exponentially with depth. Its amplitude p_1 scaled with kinetic energy of the turbulent flow such that $p_1^* \equiv [p_1/(\rho U^2)](\lambda/h_0) = 2.19 \pm 0.14$, a value smaller than what *Louge et al.* [2010a] had assumed for calculating seepage, dust, and humidity penetration in desert ripples. On the surface, the dimensionless pressure was nearly dentical in phase and amplitude to earlier measurements of *Kendall* [1970] on an impermeable sinusoidal wall, thus suggesting that the porous subtrate is relatively unimportant to surface pressure evolution at that aspect ratio. We showed that because surface and pore pressure scale with h_0/λ, and because the flow mostly did not separate behind crests, these measurements were also relevant to any sinusoidal ripple with $h_0/\lambda \leqslant 3\%$ (i.e., RI $\gtrsim 16$).

Experiments at $h_0/\lambda = 6\%$ exhibited an asymmetric pore pressure distribution suggesting flow separation behind ripple crests and possible reattachment before the next trough. For this aspect ratio, we compared the evolution of surface pressure on our porous substrate with published data on similar impermeable sinusoidal ripples [*Buckles et al.*, 1984; *Gong et al.*, 1996; *Henn and Sykes*, 1999]. While the dimensionless depression that we measured at the crest was identical to those earlier results, we noted a sharp attenuation of surface pressure upwind of the crest, suggesting that the porous medium imposes a markedly different surface pressure gradient on the turbulent boundary layer than on comparable impermeable ripples. By invoking observations of *Gong et al.* [1996] on aerodynamically smooth and rough impermeable ripples, we attributed this attenuation to the retrodiffusion of pore pressure through the bed. Using the boundary condition of *Beavers and Joseph* [1967], we calculated that the porous bed also allows a substantial slip velocity to arise on the surface, further affecting turbulence in the main flow. For simplicity, we regarded such slip as an effective reduction in aerodynamic roughness.

Although pressure drag appeared to increase with $\rho U^2 h_0^2/\lambda$, it was significantly smaller than its counterpart on impermeable wavy surfaces [*Gong et al.*, 1996; *Buckles et al.*, 1984; *Henn and Sykes*, 1999]. At $h_0/\lambda = 6\%$, this pressure drag reduction could also be attributed to surface pressure attenuation by retrodiffusion. We recorded a lift force on the ripple surface that appeared to increase $\propto \rho U^2 h_0^3/\lambda^2$, although such scaling should be confirmed with new porous rigs at greater h_0/λ. Finally, we also noted that ripples with $h_0/\lambda = 6\%$ exhale a net amount of air, while ripples of $h_0/\lambda = 3\%$ do not.

Our measurements were sufficiently accurate to evaluate pore pressure gradients ∇p and thus to gauge where the latter might defeat gravity and mobilize a bed of uniform volume fraction ν and grain material density ρ_s. The onset of mobilization arises when $F\mathbb{R} > 1$, where the number $\mathbb{R} \equiv \rho U^2 h_0/(\rho_s \nu g \lambda^2)$ regroups wind and bed parameters. Ignoring internal friction, $F \equiv (\partial p/\partial y)\,\lambda^2/(\rho U^2 h_0)$ peaks at $F_{\max} \simeq 17$ for $h_0/\lambda = 3\%$ and at the surprisingly similar value $F_{\max} \simeq 15$ for 6%. For the smaller aspect ratio, the peak is reached near the crest; for the larger one, $F_{\max}$ arises at a distance $\simeq \lambda/10$ upstream of that point, nearby where the theory of *Jackson and Hunt* [1975] also places the peak shear stress.

Exploiting our measurements and recalling the correlation of *Shao and Lu* [2000] for threshold velocity in aeolian transport, we calculated that pressure gradient-induced fluidization of the porous bed would occur before shear-induced erosion of surface grains of diameter d whenever $\sqrt{h_0 d}/\lambda > 0.054$. While this criterion is rarely observed in aeolian ripples with relatively small h_0/λ [*Tanner*, 1967], our measurements suggest that it may contribute to the shaping of megaripples with high aspect ratios and coarse surface grains. Because this criterion is independent of fluid properties, aqueous ripples may also owe their mobilization, at least in part, to pore pressure gradients within the underlying bed.

Finally, because ripples are generally asymmetrical unless their aspect ratio h_0/λ is small [*Baas*, 1994], future experiments should be conducted with cross sections of various asymmetry [*Tanner*, 1967], beginning with triangular shapes [*Blois et al.*, 2014]. Because to our knowledge there are no data for the pressure evolution on impermeable bed forms of triangular cross section, these future experiments will have to involve both porous and solid surfaces to discern the role of porosity. In this context, some useful insight might be found in the literature on "k-type roughness," in which the ratio w/k of "cavity length" $w \sim \lambda/2$ to "cavity height" $k \sim 2h_0$ exceeds 3 (or, in our notation, $h_0/\lambda < 1/12$) [*Perry et al.*, 1969; *Leonardi et al.*, 2007]. Nonetheless, we would expect that the porous medium will play a similar role on a triangular ripple than it does on a sinusoidal one, namely, that porosity should induce seepage through the bed, thus attenuating the surface pressure gradient and allowing slip at the surface.

In conclusion, our wind tunnel experiments suggested that for ripples of large amplitude relative to wavelength, bed porosity disrupts surface pressure gradients by allowing pore pressure to retrodiffuse through the bed and by establishing a slip velocity at the surface. For ripples of smaller relative amplitude, the data showed that bed porosity matters less to surface pressure. It also established the magnitude of pressure variations, which govern seepage through the bed and the possible capture of aeolian dust beneath ripple troughs. Finally, our experiments implied that seepage-induced fluidization may contribute to the shaping of megaripples with high aspect ratios and coarse surface grains.

Acknowledgments
We are grateful to Brian Mittereder, Amin Younes, and Frank Parish for manufacturing the artificial rippled surfaces; to Cian Carroll, Daniel Balentine, and Matthew Pizzonia for conducting experiments with them; to Albert George for his advice with wind tunnel operations; to Fernando Porte-Agel, Alexandre Valance, Philippe Claudin, Klaus Kroy, Peter Diamessis, and Blair Anne Johnson for illuminating discussions; and to Alexander Densmore, Bryn Hubbard, Douglas Sherman, and anonymous reviewers for their careful reading of the manuscript. Data presented in this article are archived as supporting information. This paper was made possible by the support of NPRP grant 09-546-2-206 from the Qatar National Research Fund. The statements made herein are solely the responsibility of the authors.

References

Andreotti, B., P. Claudin, and O. Pouliquen (2006), Aeolian sand ripples: Experimental study of fully developed states, *Phys. Rev. Lett.*, *96*, 028001, doi:10.1103/PhysRevLett.96.028001.

Baas, J. H. (1994), A flume study on the development and equilibrium morphology of current ripples in very fine sand, *Sedimentology*, *41*, 185–209.

Bagnold, R. (1935), The movement of desert sand, *Geog. J.*, *85*, 342–365.

Bagnold, R. A. (1942), *The Physics of Blown Sand and Desert Dunes*, William Morrow & Co., New York.

Beavers, G. S., and D. D. Joseph (1967), Boundary conditions at a naturally permeable wall, *J. Fluid Mech.*, *30*, 197–207.

Blois, G., J. L. Best, G. H. Sambrook Smith, and R. J. Hardy (2014), Effect of bed permeability and hyporheic flow on turbulent flow over bed forms, *Geophys. Res. Lett.*, *41*, 6435–6442, doi:10.1002/2014GL060906.

Boulton, A. J., S. Findlay, P. Marmonier, E. H. Stanley, and H. M. Valett (1998), The functional significance of the hyporheic zone in streams and rivers, *Annu. Rev. Ecol. Syst.*, *29*, 59–81.

Buckles, J., T. J. Hanratty, and R. J. Adrian (1984), Turbulent flow over large-amplitude wavy surfaces, *J. Fluid Mech.*, *140*, 27–44.

Cardenas, M. B., and J. L. Wilson (2007), Dunes, turbulent eddies, and interfacial exchange with permeable sediments, *Water Resour. Res.*, *43*, W08412, doi:10.1029/2006WR005787.

Carroll, C. S., M. Y. Louge, and B. Turnbull (2013), Frontal dynamics of powder snow avalanches, *J. Geophys. Res. Earth Surf.*, *118*, 913–924, doi:10.1002/jgrf.20068.

Chan, H. C., W. C. Huang, J. M. Leu, and C. J. Lai (2007a), Macroscopic modeling of turbulent flow over a porous medium, *Int. J. Heat Fluid Flow*, *28*, 1157–1166, doi:10.1016/j.ijheatfluidflow.2006.10.005.

Chan, H. C., J. M. Leu, C. J. Lai, and Y. Jia (2007b), Turbulent flow over a channel with fluid-saturated porous bed, *J. Hydraul. Eng.*, *133*, 610–617, doi:10.1061/ASCE0733-94292007133:6610.

Charru, F., B. Andreotti, and P. Claudin (2013), Sand ripples and dunes, *Annu. Rev. Fluid Mech.*, *45*, 469–93, doi:10.1146/annurev-fluid-011212-140806.

Creyssels, M., P. Dupont, A. Ould el-Moctar, A. Valance, I. Cantat, J. T. Jenkins, J.-M. Pasini, and K. R. Rasmussen (2009), Saltating particles in a turbulent boundary layer: Experiment and theory, *J. Fluid Mech.*, *625*, 47–74, doi:10.1017/S0022112008005491.

Csahók, Z., C. Misbah, F. Rioual, and A. Valance (2000), Dynamics of aeolian sand ripples, *Eur. Phys. J. E*, *3*, 71–86.

Durán, O., P. Claudin, and B. Andreotti (2011), On aeolian transport: Grain-scale interactions, dynamical mechanisms and scaling laws, *Aeolian Res.*, *3*, 243–270, doi:10.1016/j.aeolia.2011.07.006.

Elliott, A. H., and N. H. Brooks (1997), Transfer of nonsorbing solutes to a streambed with bed forms: Laboratory experiments, *Water Resour. Res.*, *33*, 137–151.

Engelund, F., and J. Fredsøe (1982), Sediment ripples and dunes, *Annu. Rev. Fluid Mech.*, *14*, 13–37.

Everitt, B. S. (2006), *Cambridge Dictionary of Statistics*, 3rd ed., Cambridge Univ. Press, Cambridge, U. K.

Foster, D. L., A. J. Bowen, R. A. Holman, and P. Natoo (2006), Field evidence of pressure gradient induced incipient motion, *J. Geophys. Res.*, *111*, C05004, doi:10.1029/2004JC002863.

Fourrière, A. (2009), River morphodynamics: Width selection, ripples and dunes, PhD thesis, Université Paris Diderot, Paris, France.

Fourrière, A., P. Claudin, and B. Andreotti (2010), Bedforms in a turbulent stream: Formation of ripples by primary linear instability and of dunes by nonlinear pattern coarsening, *J. Fluid Mech.*, *649*, 287–328, doi:10.1017/S0022112009993466.

Frederick, K. A., and T. J. Hanratty (1988), Velocity measurements for a turbulent nonseparated flow over solid waves, *Exp. Fluids*, *6*, 477–486.

Fries, J. S., and G. L. Taghon (2010), Particle fluxes into permeable sediments: Comparison of mechanisms mediating deposition, *J. Hydraul. Eng.*, *136*, 214–221, doi:10.1061/ASCEHY.1943-7900.0000169.

Gong, W., P. A. Taylor, and A. Dörnbrack (1996), Turbulent boundary-layer flow over fixed aerodynamically rough two-dimensional sinusoidal wave, *J. Fluid Mech.*, *312*, 1–31.

Goossens, D. (1988), The effect of surface curvature on the deposition of loess: A physical model, *Catena*, *15*, 179–194.

Günther, A., and P. R. von Rohr (2003), Large-scale structures in a developed flow over a wavy wall, *J. Fluid Mech.*, *478*, 257–285.

Henn, D. S., and R. I. Sykes (1999), Large-eddy simulation of flow over wavy surfaces, *J. Fluid Mech.*, *383*, 75–112.

Hersen, P. (2004), On the crescentic shape of barchan dunes, *Eur. Phys. J. B*, *37*, 507–514.

Hinze, J. O. (1975), *Turbulence*, 2nd ed., Mc-Graw-Hill, New York.

Huettel, M., P. L. M. Cook, F. Janssen, G. Lavik, and J. J. Middelburg (2007), Transport and degradation of a dinoflagellate bloom in permeable sublittoral sediment, *Mar. Ecol. Prog. Ser.*, *340*, 139–153.

Iverson, R. M. (2005), Regulation of landslide motion by dilatancy and pore pressure feedback, *J. Geophys. Res.*, *110*, F02015, doi:10.1029/2004JF000268.

Iverson, R. M., M. E. Reid, M. Logan, R. G. LaHusen, J. W. Godt, and J. P. Griswold (2011), Positive feedback and momentum growth during debris-flow entrainment of wet bed sediment, *Nat. Geosci.*, *4*, 116–121, doi:10.1038/ngeo1040.

Jackson, P. S., and J. C. R. Hunt (1975), Turbulent wind flow over a low hill, *Q. J. R. Meteorol. Soc.*, *101*, 929–955.

Jones, I. P. (1973), Low Reynolds number flow past a porous spherical shell, *Proc. Cambridge Philos. Soc.*, *73*, 231–238.

Kendall, J. M. (1970), The turbulent boundary layer over a wall with progressive surface waves, *J. Fluid Mech.*, *41*, 259–281.

Kim, H. T., S. J. Kline, and W. C. Reynolds (1971), The production of turbulence near a smooth wall in a turbulent boundary layer, *J. Fluid Mech.*, *50*, 133–160.

Kroy, K., G. Sauermann, and H. J. Herrmann (2002), Minimal model for sand dunes, *Phys. Rev. Lett.*, *88*, 054301.

Kuzan, J. D, T. J. Hanratty, and R. J. Adrian (1989), Turbulent flows with incipient separation over solid waves, *Exp. Fluids*, *7*, 88–98.

Leonardi, S., P. Orlandi, and R. A. Antonia (2007), Properties of d- and k-type roughness in a turbulent channel flow, *Phys. Fluids*, *19*, 125101, doi:10.1063/1.2821908.

Loezos, P. N., P. Costamagna, and S. Sundaresan (2002), The role of contact stresses and wall friction on fluidization, *Chem. Eng. Sci.*, *57*, 5123–5141.

Louge, M. Y., C. S. Carroll, and B. Turnbull (2011), Role of pore pressure gradients in sustaining frontal particle entrainment in eruption currents: The case of powder snow avalanches, *J. Geophys. Res.*, *116*, F04030, doi:10.1029/2011JF002065.

Louge, M. Y., A. Valance, A. Ould el-Moctar, and P. Dupont (2010a), Packing variations on a ripple of nearly monodisperse dry sand, *J. Geophys. Res.*, *115*, F02001, doi:10.1029/2009JF001384.

Louge, M. Y., A. Valance, H. Mint Babah, J.-C. Moreau-Trouvé, A. Ould el-Moctar, and D. Ould Ahmedou (2010b), Seepage-induced penetration of water vapor and dust beneath ripples and dunes, *J. Geophys. Res.*, *115*, F02002, doi:10.1029/2009JF001385.

Manes, C., D. Poggi, and L. Ridolphi (2011), Turbulent boundary layers over permeable walls: Scaling and near-wall structure, *J. Fluid Mech.*, *687*, 141–170, doi:10.1017/jfm.2011.329.

Manes, C., D. Pokrajac, I. McEwan, and V. Nikora (2009), Turbulent structure of open channel flows over permeable and impermeable beds: A comparative study, *Phys. Fluids*, *21*, 125109, doi:10.1063/1.3276292.

Manukyan, E., and L. Prigozhin (2009), Formation of aeolian ripples and sand sorting, *Phys. Rev. E*, *79*, 031303, doi:10.1103/PhysRevE.79.031303.

Meysman, F. J. R., O. S. Galaktionov, P. L. M. Cook, F. Janssen, and M. Huettel (2007), Quantifying biologically and physically induced flow and tracer dynamics in permeable sediments, *Biogeosciences*, *4*, 627–646.

Mooney, M. (1951), The viscosity of a concentrated suspension of spherical particles, *J. Colloid Sci.*, *6*, 162–170.

Mutlu Sumert, B., and M. Bakioglu (1984), On the formation of ripples on an erodible bed, *J. Fluid Mech.*, *144*, 177–190.

Nield, D. A. (2009), The Beavers-Joseph boundary condition and related matters: A historical and critical note, *Transp. Porous Media*, *78*, 537–540, doi:10.1007/s11242-009-9344-y.

Olsthoorn, J., M. Stastna, and N. Soontiens (2012), Fluid circulation and seepage in lake sediment due to propagating and trapped internal waves, *Water Resour. Res.*, *48*, W11520, doi:10.1029/2012WR012552.

Packman, A. I., M. Salehin, and M. Zaramella (2004), Hyporheic exchange with gravel beds: Basic hydrodynamic interactions and bedform-induced advective flows, *J. Hydraul. Eng.*, *130*, 647–656, doi:10.1061/(ASCE)0733-9429(2004)130:7(647).

Perry, A. E., W. H. Schofield, and P. N. Joubert (1969), Rough wall turbulent boundary layers, *J. Fluid Mech.*, *37*, 383–413.

Prinos, P., D. Sofialidis, and E. Keramaris (2003), Turbulent flow over and within a porous bed, *J. Hydraul. Eng.*, *129*, 720–733, doi:10.1061/(ASCE)0733-9429(2003)129:9(720).

Pye, K., and H. Tsoar (1987), The mechanics and geological implications of dust transport and deposition in deserts with particular reference to losess formation and dune sand diagenesis in the northern Negev, Israel, in *Desert Sediments: Ancient and Modern,* edited by L. Frostick and I. Reid, *Geol. Soc. Spec. Publ., 35*, 139–156.

Ribando, R. J. (1974), The Cornell environmental wind tunnel, MS thesis, Cornell Univ., 1–140, Ithaca, New York.

Richards, K. L. (1980), The formation of ripples and dunes on an erodible bed, *J. Fluid Mech.*, *99*, 697–618.

Roche, O., S. Montserrat, Y. Niño, and A. Tamburrino (2010), Pore fluid pressure and internal kinematics of gravitational laboratory air-particle flows: Insights into the emplacement dynamics of pyroclastic flows, *J. Geophys. Res.*, *115*, B09206, doi:10.1029/2009JB007133.

Saffman, P. G. (1971), On the boundary condition at the interface of a porous medium, *Stud. Appl. Math.*, *1*, 93–101.

Shao, Y., and H. Lu (2000), A simple expression for wind erosion threshold friction velocity, *J. Geophys. Res.*, *105*, 22,437–22,443.

Sherman, D. J., and E. J. Farrell (2008), Aerodynamic roughness lengths over movable beds: Comparison of wind tunnel and field data, *J. Geophys. Res.*, *113*, F02S08, doi:10.1029/2007JF000784.

Shields, A. (1936), Anwendung der Aehnlichkeitsmechanik und der Turbulenzforschung auf die Geschiebebewegung (Application of similarity principles and turbulence research to bedload motion), *Mitteilungen der Preußischen Versuchsanstalt für Wasserbau*, 26, Berlin, pp. 1–26.

Sleath, J. F. A. (1999), Conditions for plug formation in oscillatory flow, *Cont. Shelf Res.*, *19*, 1643–1664.

Sophocleous, M. (2002), Interactions between groundwater and surface water: The state of the science, *Hydrogeol. J.*, *10*, 52–67.

Tanner, W. F. (1967), Ripple mark indices and their uses, *Sedimentology*, *9*, 89–104.

Thorsness, C. B., P. E. Morrisroe, and T. J. Hanratty (1978), A comparison of linear theory with measurements of the variation of shear stress along a solid wave, *Chem. Eng. Sci.*, *33*, 579–592.

Tsinontides, S. C., and R. Jackson (1993), The mechanics of gas fluidized beds with an interval of stable fluidization, *J. Fluid Mech.*, *255*, 237–274.

Willmarth, W. W. (1975), Pressure fluctuations beneath turbulent boundary layers, *Annu. Rev. Fluid Mech.*, *7*, 13–36.

Yizhaq, H., I. Katra, J. F. Kok, and O. Isenberg (2012), Transverse instability of megaripples, *Geology*, *40*, 459–462, doi:10.1130/G32995.1.

Zedler, E. A., and R. L. Street (2001), Large-eddy simulations of sediment transport: Currents over ripples, *J. Hydraul. Eng.*, *127*, 444–452.

Zilker, D. P., and T. J. Hanratty (1979), Influence of the amplitude of a solid wavy wall on a turbulent flow: Part 2. Separated flows, *J. Fluid Mech.*, *90*, 257–271.